

How water and ion mobility affect the NMR fingerprints of the hydrated JBW zeolite: a combined computational-experimental investigation

Supporting Information

Siebe Vanlommel^[a], Alexander E.J. Hoffman^[a], Sam Smet^[b], Sambhu Radhakrishnan^[b,c], Karel Asselman^[b], C. Vinod Chandran^[b,c], Eric Breynaert^[b,c,d], Christine E.A. Kirschhock^[b], Johan A. Martens^[b,c], and Veronique Van Speybroeck^{[a]*}

E-mail: Veronique.VanSpeybroeck@UGent.be

^[a]Center for Molecular Modeling, Ghent University, Technologiepark 46, 9052 Ghent, Belgium

^[b]Center for Surface Chemistry and Catalysis, KU Leuven, Celestijnenlaan 200f, PO Box 2461, 3001 Leuven, Belgium

^[c] NMR-Xray platform for Convergence Research (NMRCoRe), KU Leuven, Celestijnenlaan 200f, PO Box 2461, 3001 Leuven, Belgium

^[d] National High Magnetic Field Laboratory, 1800 E. Paul Dirac Dr., Tallahassee FL 32310, United States

Contents

S1 Experimental NMR details	S.2
S2 Computational methodology	S.4
S3 Shift-shielding relation	S.9
S4 Additional NMR data: asymmetry parameter and ^{29}Si NMR	S.12
Triclinic system	S.12
Orthorhombic system	S.12
S5 Average T-O-T angle	S.15
S6 Al-K pair distribution functions	S.16
S7 ^{23}Na and ^{39}K NMR	S.16
S8 Lattice parameters & symmetry breaking	S.19
S9 Convergence tests	S.20
Computational settings for DFT-GIPAW	S.20
Convergence of NMR parameters in time	S.22
S10 Averaging over T-sites and space group transformations	S.24
S11 Structural models and input files	S.25
References	S.27

S1 Experimental NMR details

Details for the experimental NMR spectral collection were as follows. ^{27}Al and ^1H solid-state NMR experiments were performed on a Bruker Avance III 500 MHz NMR spectrometer (9.4

T) equipped with a 4 mmH/X/Y solid state MAS probe. Larmor frequencies were 130.52 and 500.87 MHz for ^{27}Al and ^1H , respectively. The samples were put in a 4mm ZrO_2 rotor and spun at 15 kHz MAS frequency. ^1H NMR spectra were acquired with an 83 kHz RF pulse, recycle delay of 5 s, and 8 transients. A total of 1024 scans (recycle delay of 2 s) were recorded for ^{27}Al MAS NMR with ^1H decoupling using the SWf-SPINAL method. The RF strengths used for ^{27}Al and ^1H for decoupling are 150 kHz and 55 kHz, respectively. ^{27}Al spectra were recorded using a 15°flip angle. For Z-filtered ^{27}Al MQMAS measurements, 600 slices in the indirect dimension were acquired with a t1 increment of 33.33 μs , a relaxation delay of 2 s, and 60 transients in the direct dimension. ^{29}Si MAS NMR experiments were carried out on a Bruker Avance III 300 MHz NMR spectrometer (7.1 T) equipped with a 4 mm H/X solid-state MAS probe. The ^{29}Si Larmor frequency was 59.62 MHz. The MAS frequency used was 10 kHz. The RF strengths used for ^{29}Si excitation and ^1H decoupling were 66 and 40 kHz, respectively. A total of 320 transients were collected with 600 s of recycle delay. ^{23}Na measurements were performed on a Bruker Ascend 800 MHz (18.8 T) equipped with a 1.9mm H/X/Y probe. The sample was put in a 1.9 mm ZrO_2 rotor and spun at 30 kHz. The RF strengths used were 110 kHz on ^{23}Na and 19kHz on ^1H for decoupling. ^{29}Si chemical shifts were referenced to a secondary reference, Q8M8, which was further referenced against a primary reference, tetramethylsilane (TMS). ^{27}Al chemical shifts were referenced against 0.1 M solutions of $\text{Al}(\text{NO}_3)_3$. ^{23}Na spectra were referenced to 0.1 M NaCl solution in D_2O . All of the ^{39}K MAS NMR experiments were carried out on a Bruker 830 MHz NMR spectrometer at the National High Magnetic Field Laboratory (Tallahassee, Florida) operating at a 19.6 T magnetic field and with a ^{39}K Larmor frequency of 38.80 MHz. The samples were packed in 3.2 mm zirconia rotors and spun up to 20 kHz. QCPMG (Quadrupolar Carr-Purcell-Meiboom-Gill) signals with 9 to 12 echoes for the three samples were acquired, yielding the spikelet pattern after Fourier transformation. The excitation and refocusing pulses for the QCPMG sequence are 4 and 8 μs , respectively. A range of 247000 to 1835000 transients were recorded for all experiments. A WURST (Wideband-

Uniform Rate-Smooth Truncation) pulse lasting 32 rotor periods (1.6 ms) with a 200kHz offset and a nutation frequency of 28 kHz was applied to the satellite transitions to enhance the central transition polarization prior to the QCPMG. The ^{39}K experiments used the ^{17}O NMR resonance of aqueous D_2O as a secondary reference using the $^{39}\text{K}/^{17}\text{O}$ spectrometer frequency (SF) interconversion: $\text{SF}(\text{K}) = \text{SF}(\text{O}) \times 4.666373 / 13.556457$ (frequency ratios calculated from the magnetogyric ratios).¹

S2 Computational methodology

The computational models were built by taking the framework Al, Si and O atoms and extraframework Na^+ and K^+ ionic positions from the XRD structures of the triclinic and orthorhombic systems. These systems serve as the anhydrous models. Subsequently, water was added in discrete steps of one water molecule to the orthorhombic system until saturation is reached. The saturation point of water adsorption in the system was determined through grand canonical Monte Carlo simulations (GCMC) to be 0.33 H_2O per aluminium atom ($\text{H}_2\text{O}/\text{Al}$), which in our system corresponds to 4 water molecules in the unit cell of 24 T-sites. For the energy evaluations needed in the GCMC method, a non-covalent force field was derived as follows. The ground state electron density was calculated with GPAW² as implemented in ASE³ using the LCAO method.⁴ Partitioning of the electron density was performed with DensPart.⁵ Lennard-Jones parameters taken from Ref.⁶ were used for the Van der Waals interactions. For water, the TIP-3P model was used.⁷ To run the GCMC simulation, the GCMC code as implemented in Python by Goeminne *et al.* was used.⁸ We thus have a system with water content ranging from zero to four water molecules per unit cell (0 to 0.33 $\text{H}_2\text{O}/\text{Al}$). Experimentally the adsorbed water content varies from 0.02 $\text{H}_2\text{O}/\text{Al}$ to 0.21 $\text{H}_2\text{O}/\text{Al}$ as determined through proton NMR. Note that the experimental value of highest adsorbed water content is lower than the computational saturation point. Experimentally, the value is underestimated due to the process of chemical exchange: as

more water is added to the system, protons can exchange between free water in the rotor and adsorbed water in the system, generally leading to an underestimation of the amount of protons present in water molecules adsorbed in the system and therefore of the amount of adsorbed water. As in the main text, we stress here that the computational saturation point corresponds to an equal amount of water molecules as potassium ions in the system, which is fully consistent with the XRD measurement that potassium ions and water molecules are alternating in the 8-ring channel. The resulting systems were then used as input for static and dynamic models to obtain the ^{27}Al and ^{29}Si NMR parameters for both triclinic and orthorhombic systems. To model the lowest possible water content of 0.02 H₂O/Al in the orthorhombic case, the same initial anhydrous structure is used in static and dynamic models, however the unit cell is forced to retain orthorhombicity. This is mandatory, as the triclinic cell is energetically more stable than the orthorhombic cell in the anhydrous case. It is unnecessary to force orthorhombicity upon the system to obtain models for the hydrated cases, as then the orthorhombic unit cell is energetically favoured over the triclinic one at any water loading (also see Section S8).

The computational workflow to obtain the NMR parameters is shown in Figure S1. The main property of interest, the isotropic chemical shift, is derived from the chemical shielding interaction. Upon applying an external magnetic field \mathbf{B}_{ext} , the magnetic field at the nucleus \mathbf{B}_{ind} is not the same as the external field due to the shielding effect of the surrounding electronic structure, characterized by the shielding tensor $\overline{\sigma}$:

$$\mathbf{B}_{\text{ind}} = -\overline{\sigma} \mathbf{B}_{\text{ext}} \quad (1)$$

The trace of the shielding tensor defines the isotropic chemical shielding σ_{iso} , which is converted to the isotropic chemical shift δ_{iso} through fitting the linear relationship between the

two properties using a set of reference structures:

$$\sigma_{\text{iso}} = \frac{1}{3} \text{Tr } \bar{\bar{\sigma}} \quad (2)$$

$$\delta_{\text{iso}} = a_{\text{ref}} \sigma_{\text{iso}} + b_{\text{ref}} \quad (3)$$

Details of the relation between the shielding and shift are provided in Section S2. The quadrupolar coupling constant and asymmetry parameter are defined by the eigenvalues of the electric field gradient (EFG) tensor evaluated at the nucleus, which can be calculated with the PAW method.^{9,10} Let V be the electrostatic potential evaluated at the nucleus and r_i ($i = 1, 2, 3$) the three cartesian components of the nuclear position. As $\bar{\bar{\sigma}}$ is traceless, the eigenvalues of the EFG tensor can be fully characterized by two parameters. These properties are the quadrupolar coupling constant and asymmetry parameter, defined as:

$$\text{EFG tensor components: } V_{ij} = \frac{\partial^2 V}{\partial r_i \partial r_j} \quad (4)$$

$$\text{Quadrupolar coupling constant: } C_Q = \frac{eQV_{ZZ}}{h} \quad (5)$$

$$\text{Quadrupolar asymmetry parameter: } \eta_Q = \frac{V_{YY} - V_{XX}}{V_{ZZ}} \quad (6)$$

where Q is the nuclear quadrupole moment, e the unit charge and h Planck's constant. V_{XX}, V_{YY}, V_{ZZ} denote the diagonal components of the EFG tensor after diagonalisation (the eigenvalues), in the convention $|V_{ZZ}| > |V_{XX}| > |V_{YY}|$. The notation XX, YY, ZZ is the conventional naming of the principal axis system, which is the coordinate system against which the EFG tensor is a diagonal matrix. The chemical shift and quadrupolar parameters are extremely sensitive to the local electronic structure and therefore to local structural features, which makes them interesting properties to investigate aluminium distributions. The NMR properties can be calculated through either a dynamic method, in which the system is followed in time and various configurations are taken into account, or a static method where a single optimized configuration is used.

In the dynamic method, the structures at different water contents generated based on the XRD structure are used as starting systems for *ab initio* molecular dynamics (AIMD) simulations performed in the *NPT* ensemble in the case of hydrated cells using the GPW method¹¹ implemented in CP2K.¹² The *NPT* ensemble employs a barostat (target pressure 1 bar) and a thermostat (target temperature 300 K),^{13,14} and therefore aims to closely reflect the experimental conditions. The trajectory for the anhydrous orthorhombic cell is sampled in the *NVT* ensemble, in which no barostat is employed and the volume and cell parameters are fixed. The anhydrous triclinic cell is sampled in the *NPT* ensemble. The computational settings for the DFT method were as follows: PBE functional^{15,16} with DFT-D3(BJ) dispersion correction,^{17,18} a plane wave cutoff of 500 Ry, Brillouin zone sampling restricted to the Gamma point in the GPW method and MOLOPT-DZ basis sets.¹⁹ From the trajectories, the chemical shieldings are calculated through the gauge-including projector augmented wave (GIPAW) method^{9,20} as implemented in VASP^{10,21–24} for a set of 25 snapshots spaced 4 ps in time. Computational settings for the GIPAW method were determined based on the convergence of the NMR properties with respect to the cutoff energy and number of K-points (see Section S5). The PBE functional was used and the DFT-D3(BJ) dispersion correction method with a cutoff of 600 eV with a K-point grid of 2x4x3 generated using the Monkhorst-Pack scheme.²⁵ For each atom in the structures, the time-average NMR properties are then calculated. The isotropic chemical shift δ_{iso} can be time-averaged directly, as it only depends on the trace of the shielding tensor $\bar{\sigma}$ which is invariant to rotations of the tensor that occur during the dynamic run. The quadrupolar parameters depend on the individual eigenvalues, therefore the time-average coupling constant and asymmetry parameter for each site are obtained by time-averaging the EFG tensor of the site and then diagonalising the time-average EFG tensor.

Where the dynamic method takes into account the effect of motional averaging, the static

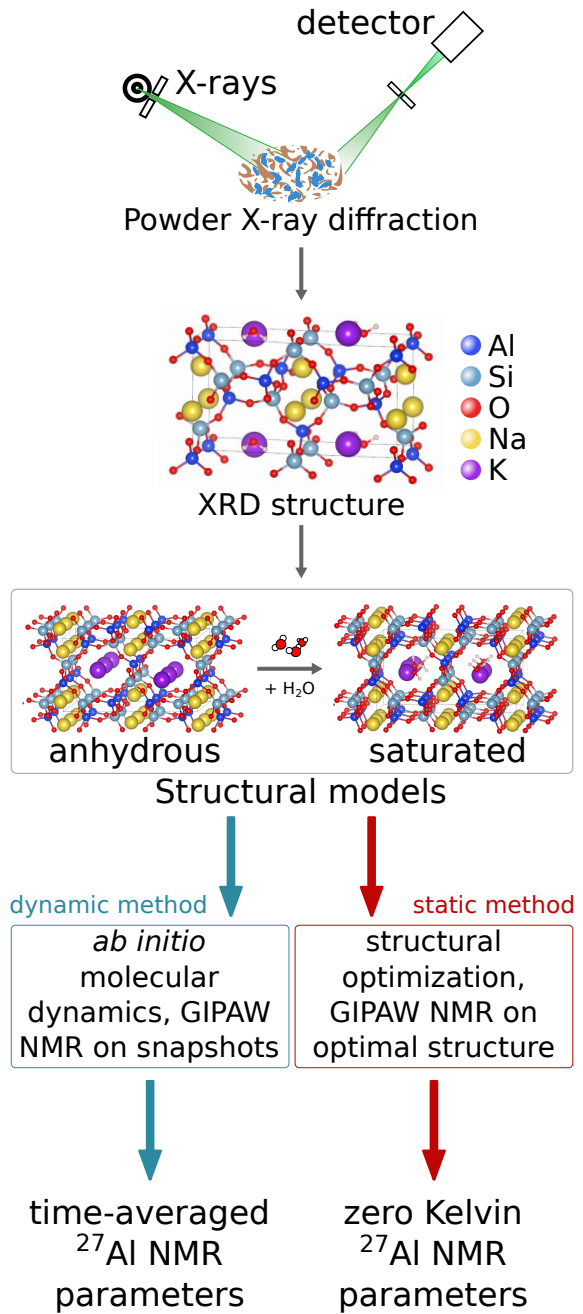


Figure S1: Outline of the static and dynamic computational schemes used in this work. The XRD structure is used as input for both static and dynamic models at different water contents. NMR parameters can then be calculated based on time-averaging over snapshots (dynamic method) or by using a single optimized structure (static method).

method uses a single optimized atomic configuration. The unit cells were optimized using VASP within the PAW formalism⁹ of DFT. Convergence criteria for the SCF steps and ionic steps were $< 10^{-8}$ eV and $< 10^{-7}$ eV, respectively. The maximal force on any atom in the optimized structures was less than 0.002 eV/Å and the average force on all the atoms in any structure was less than 0.0004 eV/Å. Using the optimized structures, the absolute shielding tensors were calculated with GIPAW. The computational settings for the optimisations and linear response GIPAW calculations were the same as those of the GIPAW calculations performed in the dynamic method. Conversion of chemical shielding values to chemical shifts was done based on fitting the linear relation that exists between these properties. Details of this procedure are explained in the following section.

S3 Shift-shielding relation

The GIPAW method in VASP calculates the isotropic magnetic shielding. The property of interest is the isotropic chemical shift, which is linearly related to the shielding through:

$$\delta_{\text{iso}} = a_{\text{ref}} \sigma_{\text{iso}} + b_{\text{ref}} \quad (7)$$

One method to convert calculated shieldings to shifts, is by fitting a_{ref} and b_{ref} to a number of reference materials. Such a linear relation must be derived for each isotope of interest. The idea is to take into account any systematic errors in the GIPAW-DFT method. At the same time, any non-systematic error (such as those due to discrepancies between structural models and experimental systems) are assumed to be non-correlated and to cancel out because the compounds are diverse in nature. The reference compounds, experimental chemical shift and calculated shieldings for ²⁷Al and ²⁹Si are shown in Table S1. The resulting relations are shown in Figure S2.

The shieldings were calculated using the static method (thus, optimizing the unit cell and atomic positions of the structures and afterwards using GIPAW to calculate the shieldings).

Table S1: Compounds containing aluminium and silicon that were used as reference structures to fit the relation between calculated shielding and shift.

isotope	compound ^{ref}	experimental shift	calculated shielding
²⁷ Al	aluminium phosphide ²⁶	142	-423.31
	andalusite ²⁷	35.5	-527.61
	potassium aluminate ²⁸	76	-487.35
	natrolite ²⁹	64.7	-500.2
	sillimanite ³⁰	63.9	-502.35
		4.7	-556.94
²⁹ Si	scolecite ³¹	62.3	-501.67
		66	-498.71
	andalusite ²⁷	-79.6	-408.54
	sillimanite ³²	-86.8	-418.24
	beta sodium disilicate ³³	-86.3	-413.53
		-88.2	-414.82
	jadeite ³³	-91.8	-421.73
	quartz ³⁴	-107.1	-437.11
	coesite ³⁴	-113.9	-446.81
		-108.1	-439.71
	ZMS-18 ³⁵	-104.27	-434.99
		-113.68	-445.47

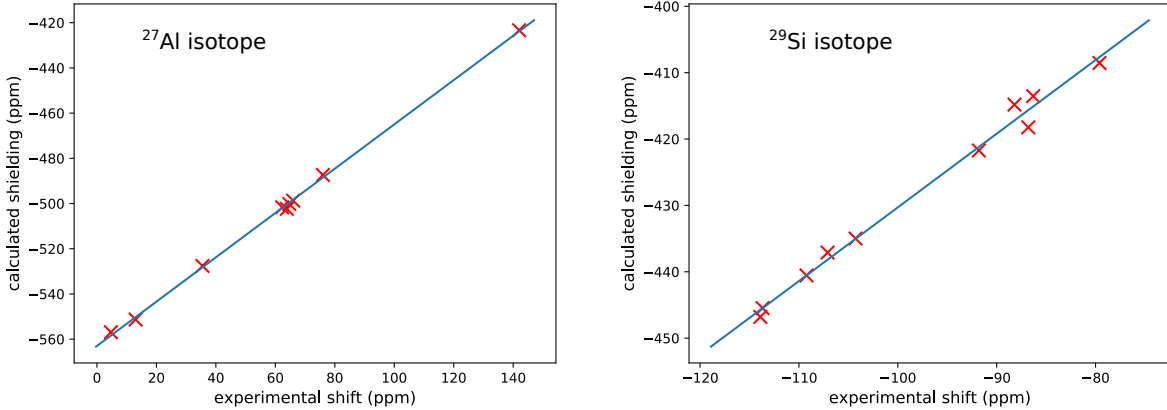


Figure S2: Calculated shieldings plotted against experimental shifts from the literature for silicon and aluminium. Inverting the relationship of the fit yields the following conversion formulas: $\delta_{\text{iso}}^{\text{Al}} = 1.02\sigma_{\text{iso}}^{\text{Al}} + 574.32 \text{ ppm}$, $\delta_{\text{iso}}^{\text{Si}} = 0.90\sigma_{\text{iso}}^{\text{Si}} + 286.96 \text{ ppm}$.

The conversion between computational shifts and shieldings in the dynamic method is done using the same relationship as in the static method, for consistency. Of course, since the static structures are optimized in VASP using the PAW method, and the dynamic snapshots are derived from a trajectory generated by CP2K using the gaussian and plane waves (GPW) method, slight discrepancies in geometry are to be expected. Therefore, for the chemical shift in the dynamic method, it is most instructive to look at the difference in chemical shift between sites (see Section 4.3). Note that the shift-shielding relation for silicon has a slope that deviates more from the theoretically exact value of 1.0 than for aluminium. We can attribute this to the fact that the shift range of the data points for silicon is smaller than for aluminium and as such the set of references for silicon is less diverse, leading to more correlated errors. However, for our purposes, this is sufficient.

S4 Additional NMR data: asymmetry parameter and ^{29}Si NMR

Triclinic system

Figure S3 contains the ^{27}Al quadrupolar asymmetry parameter plotted against the QCC and ^{29}Si chemical shifts for the static and dynamic methods and the comparison against the experimental data. The asymmetry parameter shows a very large spread and it is not very useful to distinguish between T1A, T1B and T2 sites, as e.g. T2 sites have η_Q values within the dynamic method ranging from 0.18 to 0.80. This can be explained by considering the location of potassium and the limited configurational diversity of water in the dynamic model, as is explained in the main text for the chemical shift and QCC. For ^{29}Si , the chemical shifts are more separated per label, however significant overlap is still present. The same conclusions as drawn for ^{27}Al from the main text hold for ^{29}Si .

Orthorhombic system

Figure S4 contains the ^{27}Al quadrupolar asymmetry parameter and ^{29}Si chemical shifts for the static and dynamic methods and the comparison against the experimental data. As is the case for the triclinic case, the asymmetry parameter shows a very large spread at almost all water loadings. There is a lot of overlap of η_Q for T1 and T2 sites. This shows that η_Q values of individual atoms are not extremely useful in distinguishing T-sites to compare to experimental values. There is more information in the average resonance for the T1 and T2 sites, as outlined the section ‘Bridging theory and experiment’ of the main text.

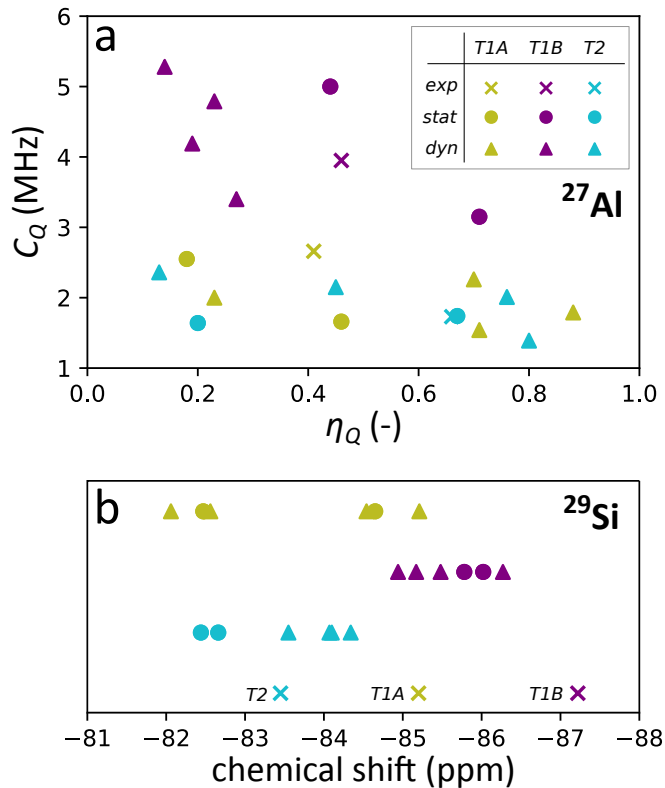


Figure S3: Additional computational data for the triclinic anhydrous case compared against experimental results. (a) ^{27}Al QCC and asymmetry parameter for the dynamic and static methods. (b) ^{29}Si chemical shift for the dynamic and static method.

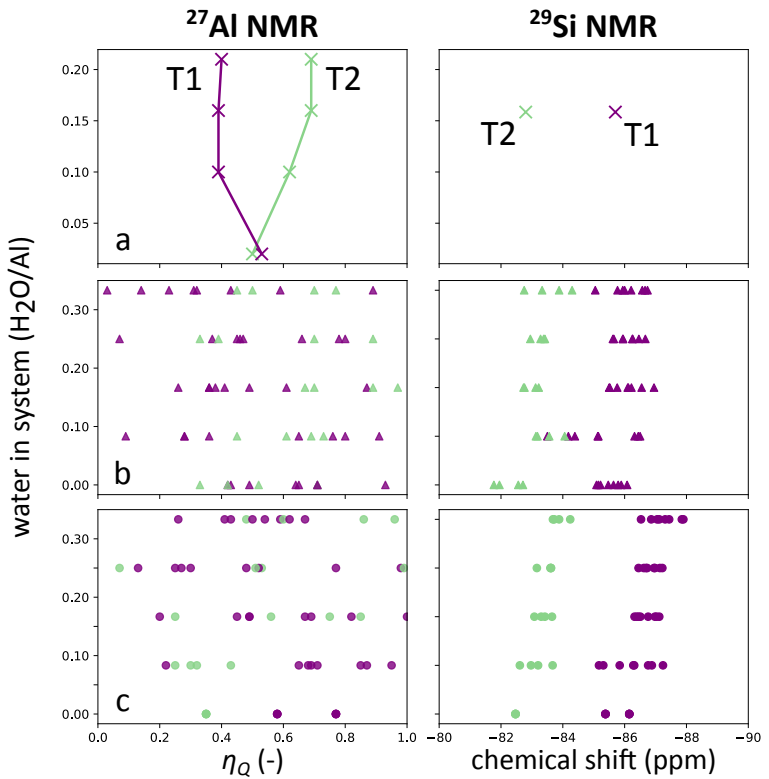


Figure S4: Additional computational data for the orthorhombic case compared against experimental results. (a) Experimental ^{27}Al quadrupolar asymmetry parameter as a function of water loading and experimental ^{29}Si chemical shift for the as-synthesised system. (b,c) Computational ^{27}Al quadrupolar asymmetry parameter and ^{29}Si chemical shifts for the dynamic (b) and static (c) methods.

S5 Average T-O-T angle

As water interacts with the framework oxygen sites, the geometry of the tetrahedrons is distorted, which results in changes in the chemical shift. Figure S5 shows the average T-O-T angle of all the T-sites in the computational systems plotted against the water loading as well as the ^{27}Al chemical shift of the T-sites. The change in the distribution of average T-O-T angles follows a similar but opposite pattern as the chemical shift (see Figure 4 of the main text for the orthorhombic data): as the amount of water is increased, the average T-O-T angles increase, whereas overall the chemical shift decreases. Moreover, there is a clear correlation between the chemical shift and the average T-O-T angle, but it shows a lot of scatter. The latter is due to the fact that the changes in chemical shift upon changes in water content cannot be explained by the changes in one particular parameter. Rather, it is a composite and complicated effect of many different geometrical parameters and the charge density as well as the motion of extraframework species and water.

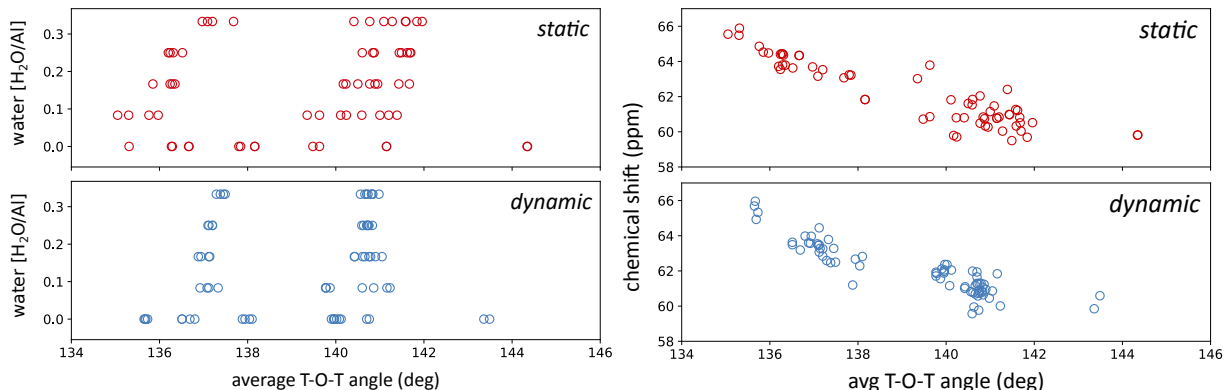


Figure S5: Average T-O-T angles in the computational systems plotted against the water content (left) and the ^{27}Al chemical shift of the aluminium T-sites (right) for both the static model (top) and the dynamic model (bottom).

S6 Al-K pair distribution functions

Figure S6 shows the Al-K pair distribution functions for the triclinic system in both the static and dynamic models. As is the case for the orthorhombic model, there is further distinction between aluminium sites within the T1A respectively T1B labels based on the different distance to the potassium ions in the static model. However, contrary to the orthorhombic model, there is not enough potassium mobility in the dynamic model to average out the difference. The result is that in the triclinic model, it is not possible to directly average out the NMR parameters to obtain representative T1A, T1B and T2 NMR resonances.

S7 ^{23}Na and ^{39}K NMR

Experimental ^{23}Na and ^{39}K MAS NMR spectra were recorded for the as-made sample and for the dehydrated sample. The comparison to ^{23}Na dynamic model data is shown in Figure S7. We note that computational sodium NMR parameters are not the goal of this study, therefore we did not derive a shift-shielding relation for sodium. The shift values are obtained through merely translating the shieldings so that the maximal shielding coincides with the largest ppm value of the lineshapes in the experimental spectrum. For the as-made sample as well as the dehydrated sample, there are two major contributions to the spectrum in ratios of approximately 1:1. The dehydrated spectrum contains an additional broad shoulder which previously was assigned to regions of the material in the outermost layers³⁶ which is not relevant in the present study. The dynamic chemical shifts are in decent agreement with the two sites, indicating that these contributions originate from the two sodium sites that are present in the anhydrous JBW condensed layer.

Figure S8 shows the ^{39}K MAS NMR spectra for as-synthesised (orthorhombic, hydrated) and dehydrated (triclinic) systems. For ^{39}K , it was not possible to reconstruct the envelope from the spikelet pattern reliably for both systems, which could indicate that potassium does not reside in clearly defined sites. Rather, it is disordered throughout the channel, which is

Al-K pair distribution functions

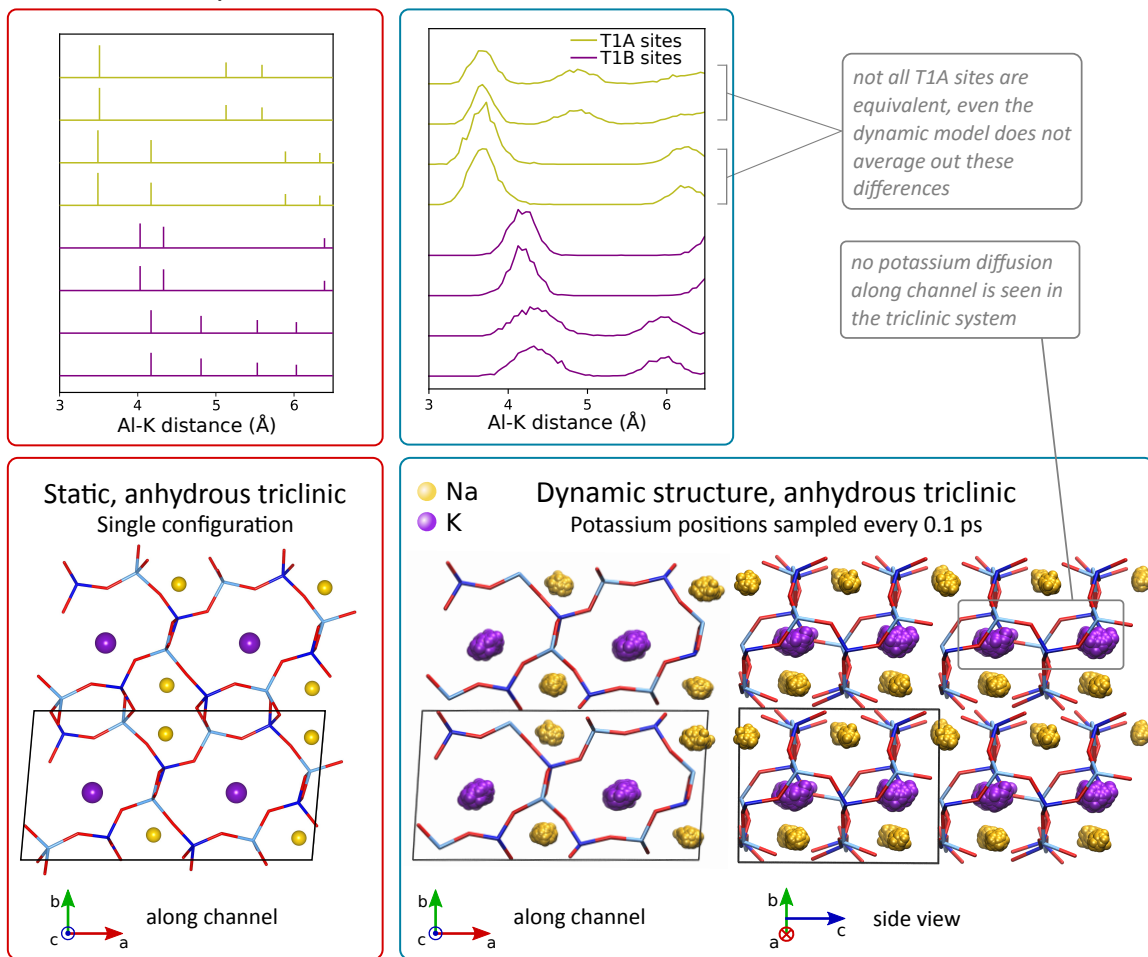


Figure S6: Static (left) and dynamic (right) Al-K pair distribution functions for the triclinic system show that further distinction within T1A and T1B sites is possible, even in using the dynamic method. The different NMR responses within these labels are not averaged out to a single value by potassium mobility as there is no diffusion throughout the system, contrary to the orthorhombic case (see main text).

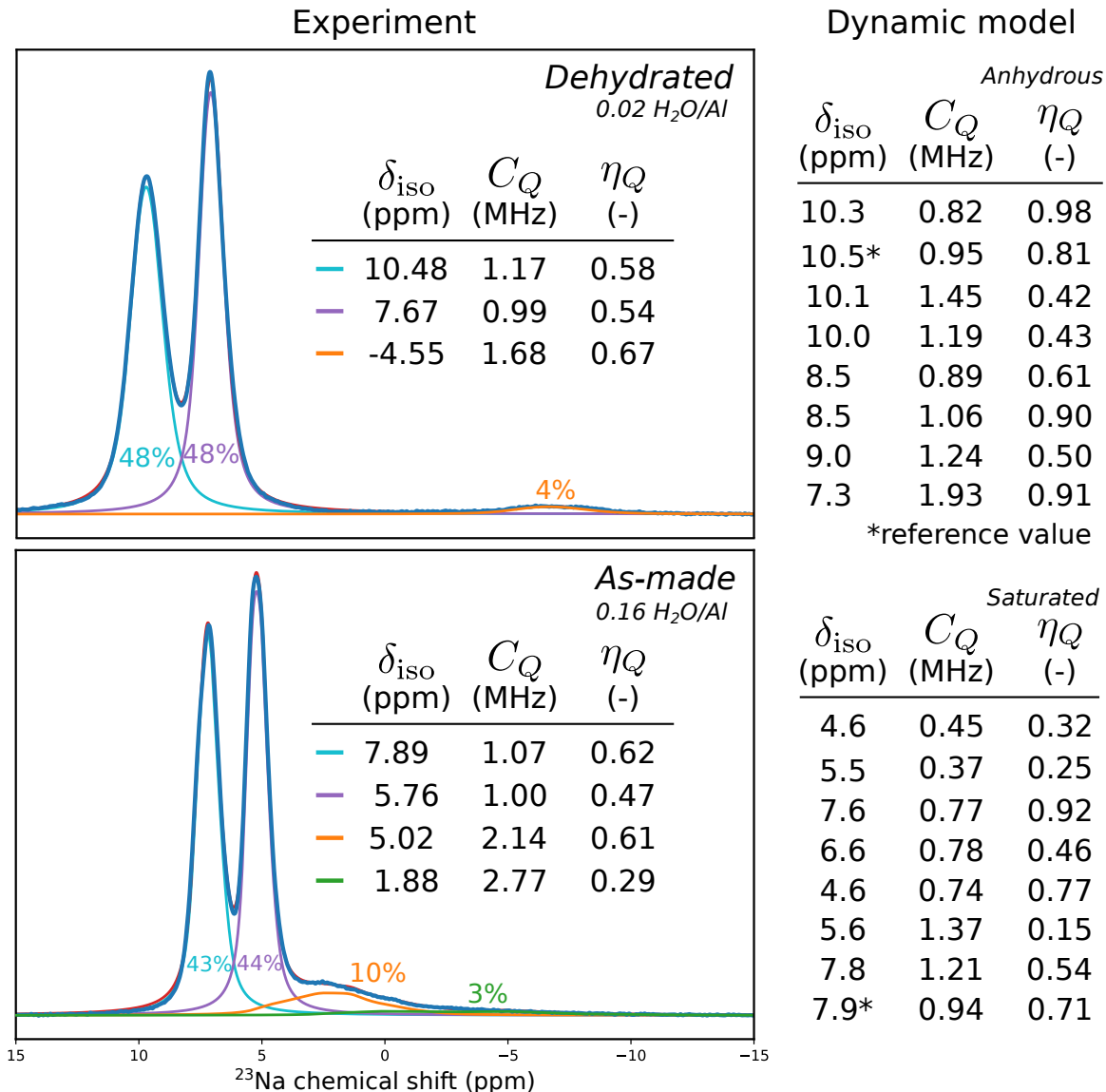


Figure S7: Experimental and dynamic model ^{23}Na (MAS) NMR data for the as-made ($0.16 \text{ H}_2\text{O}/\text{Al}$) sample and the dehydrated sample. Experimental spectrum was previously published without fitted lineshapes in Ref.³⁶

perfectly consistent with the observation that potassium is very mobile in the computational system. Computational potassium NMR data is not reported, as no quantitative data can be derived from the experimental potassium spectrum.

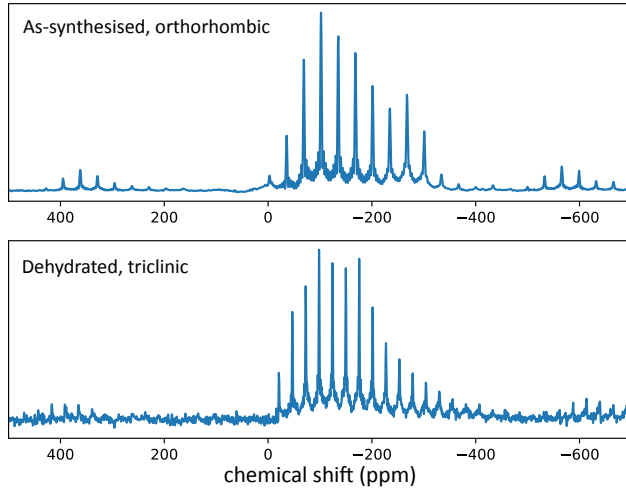


Figure S8: Experimental ^{39}K MAS NMR spectrum for the as-synthesised and dehydrated systems. These spectra were previously published in Ref.,³⁶ data may be obtained from Ref.³⁷

S8 Lattice parameters & symmetry breaking

If cell parameters are allowed to vary, the symmetry in the anhydrous cell for both the static (during geometrical optimisation) and the dynamic model (during the MD run) is broken, in agreement with experimental observation. This breaking of symmetry does not occur if any amount of water is present in the computational system, as is evidenced by the cell parameters during *NPT* MD simulations in Figure S9. Moreover, the breaking of symmetry is irreversible at room temperature: the as-made (hydrated) aluminium, sodium and silicon spectra are not recovered upon drying and rehydrating.³⁶ This is consistent with the large fluctuations in the γ cell angle that are retained if the triclinic cell is rehydrated to saturation: comparing the last two plots in Figure S9 shows that the fully orthorhombic situation is not recovered. This can be rationalised as follows. In the hydrated case, potassium ions reside in the middle of the channel and it is coordinated by a water molecule on each side

along the channel. Upon drying, water molecules are forced to break their interactions with potassium ions and the potassium ions remain undercoordinated in the channel. In the anhydrous case, potassium ions move towards the side of the channel system, thereby coordinating to framework oxygens. In this process, the framework collapses slightly and the $Pmn2_1$ symmetry is removed to retrieve the less symmetric situation of the $P\bar{1}$ space group. As both experiment and DFT simulations show, this happens spontaneously at room temperature because of the undercoordination of potassium which is not energetically preferred. Rehydrating the system is insufficient to fully recover the original $Pmn2_1$ system, because this requires removing the interactions between potassium ions and the framework oxygens, which the water molecules are unable to do at this temperature. We hypothesize that it might be possible to retrieve the original situation through heating the sample, thereby removing coordination to the framework oxygens and replacing them by coordination to water oxygens.

S9 Convergence tests

Computational settings for DFT-GIPAW

Single-point convergence tests of the absolute shielding, C_Q and η_Q parameters with respect to the energy cutoff and the number of K-points in the DFT method were performed. The results are shown in Figure S10. Settings used for the calculations were 600 eV and a K-point grid of $2 \times 4 \times 3$. All NMR parameters are very well converged with respect to these settings, and based solely on these convergence tests, lower settings would be possible. However, firstly, these high settings allow to relax the structures until very small forces are obtained in the static method (see main text). Secondly, these settings should be consistent with the settings used for the derivation of the shift-shielding relation, as to not introduce any further systematic DFT-discrepancies.

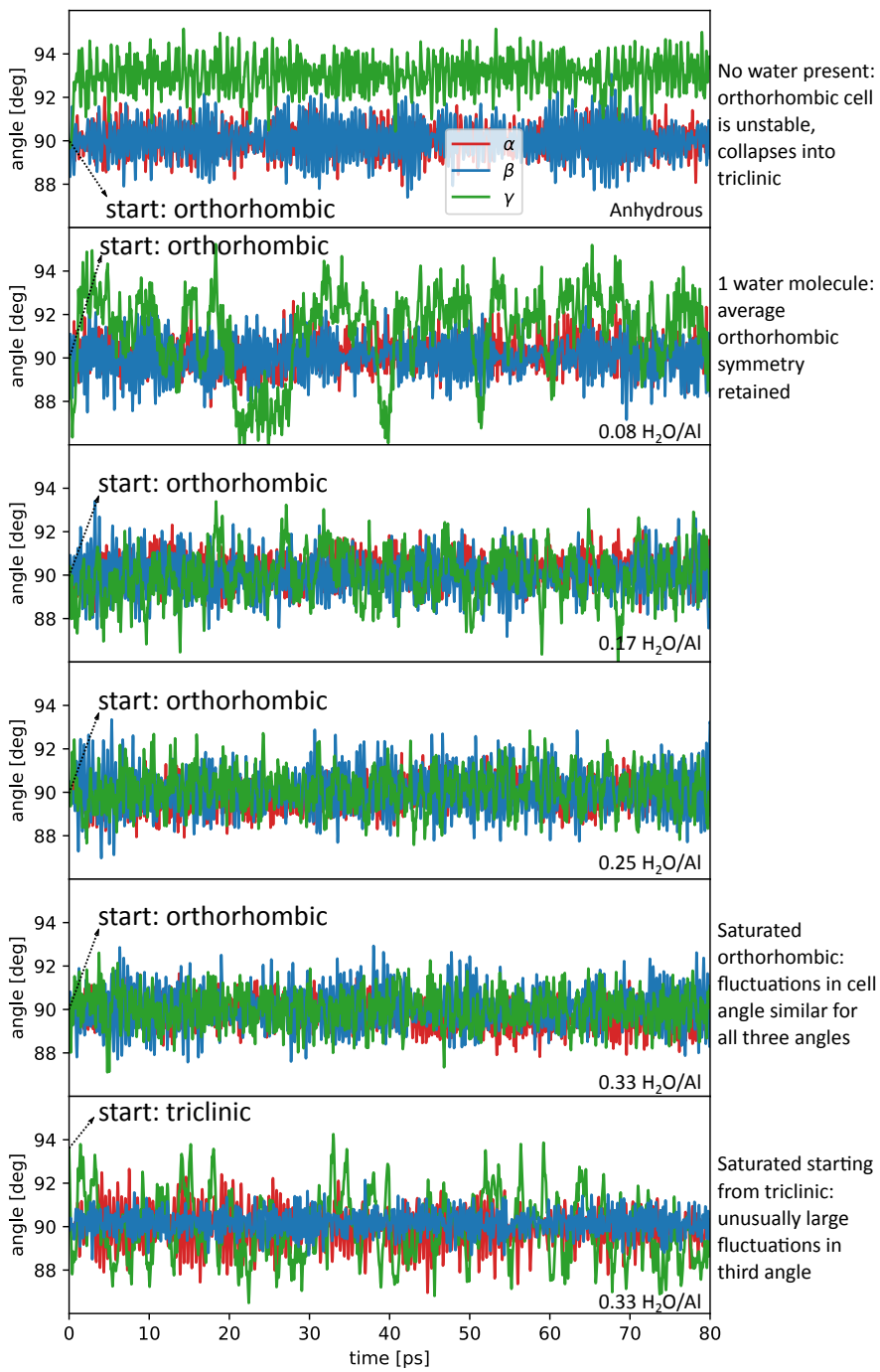


Figure S9: Unit cell angles as a function of simulation time in dynamic models for the first 80 ps of the *NPT* simulations at various water loadings. The first five plots show situations where the starting structure was orthorhombic. The bottom plot shows a rehydrated triclinic cell: this is the triclinic cell to which 4 water molecules have been added. All simulations performed at 300K and 1 bar.

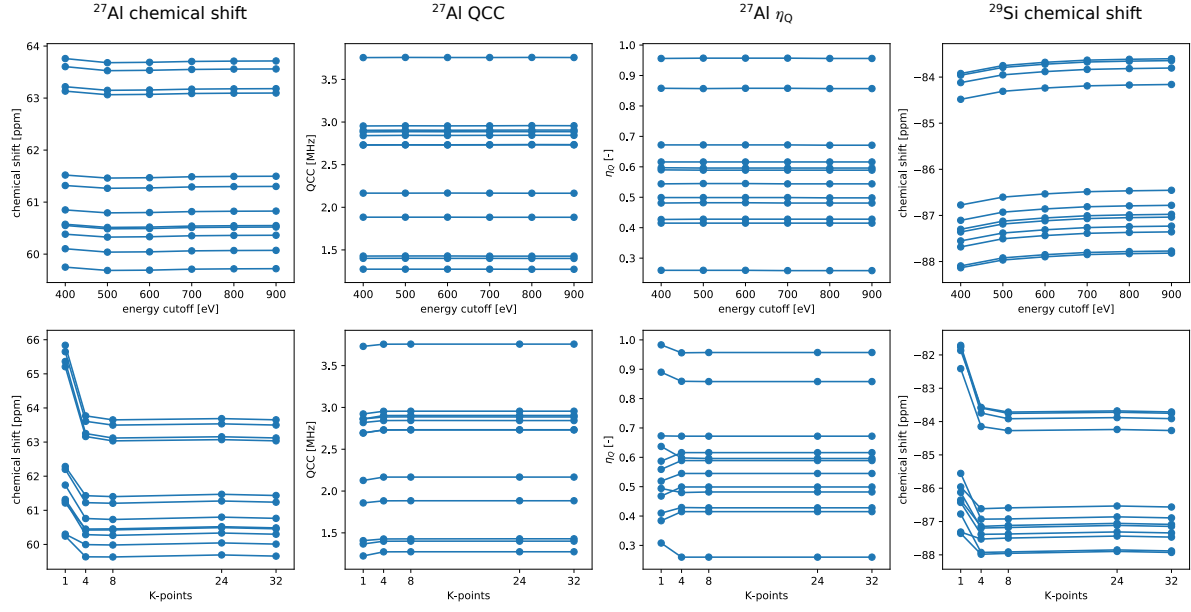


Figure S10: Single-point convergence of all NMR parameters calculated in this work with respect to cutoff energy and K-point grid.

Convergence of NMR parameters in time

The level of convergence of the NMR parameters depends on the number of MD snapshots that is used to calculate the average. The convergence of the NMR parameters of a single aluminium site with respect to the number of snapshots is shown in Figure S11. The level of convergence of this site is representative for all other sites used in the dynamic models. The convergence of the average T1/T2 NMR parameters in the saturated orthorhombic model as derived in Section 4.3 is shown in Figure S12.

Overall, the NMR parameters of the single site are converged well with respect to the number of snapshots by using about 20 snapshots. Beyond this, the change in time-average δ_{iso} , C_Q and η_Q is limited. We note that the parameter that converges the slowest is η_Q , however due to limitations in computational resources we chose not to increase simulation times any further. Moreover, as we have noted in the main text, the η_Q value of individual aluminium sites shows a large spread, which leads us to believe that this parameter has little

meaning if insufficient water configurations are taken into account. Generally, we recommend using at least 20 snapshots. Turning to the data in Figure S12, it is clear that all average T1/T2 parameters are well-converged. The average values of δ_{iso} and C_Q converge more quickly than those for individual sites, as the average T1/T2 parameters are composed of averages over multiple sites. Again, η_Q converges the slowest. Increasing the simulation time could be beneficiary for the comparison to experimental T1/T2 values, as the average η_Q of T1 sites of 0.30 at 25 snapshots seems to be still rising slightly while the experimental value is 0.40. However, for our purposes, the level of convergence is sufficient, as a difference of 0.10 in η_Q only changes the produced NMR lineshape slightly.

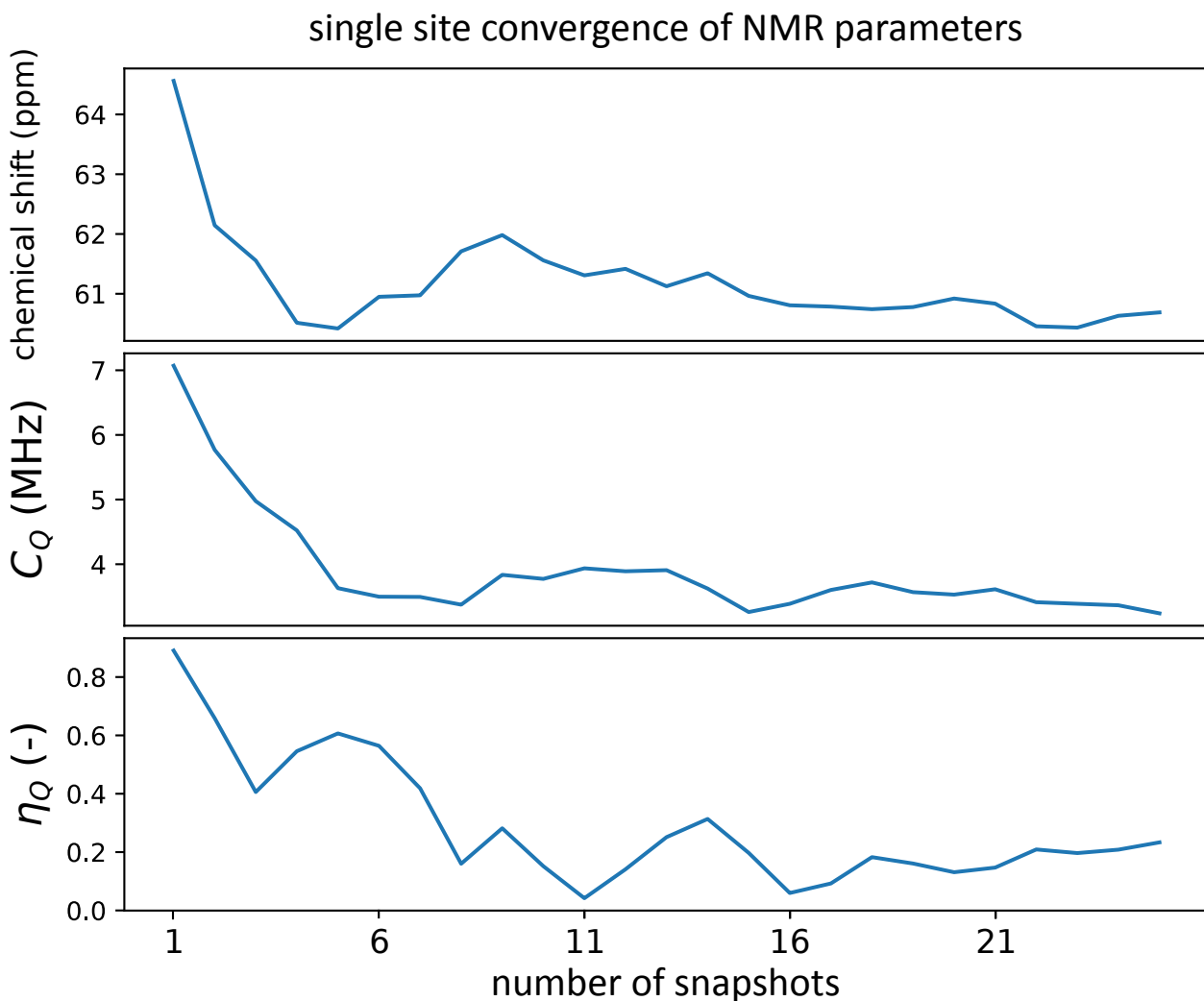


Figure S11: Convergence with respect to the number of snapshots of single aluminium site NMR parameters. Orthorhombic hydrated model at saturation (dynamic).

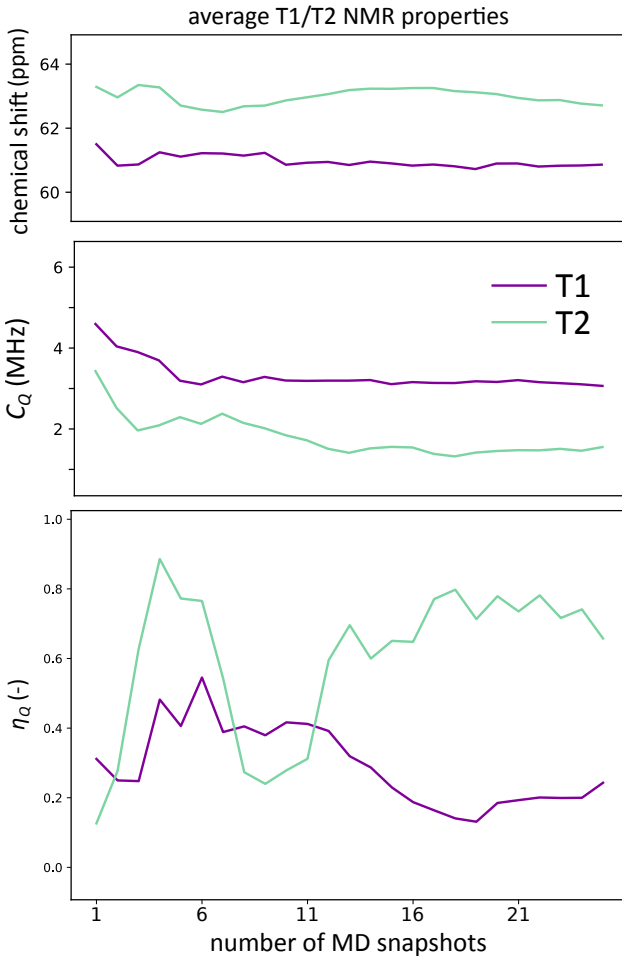


Figure S12: Convergence with respect to the number of snapshots of average T1/T2 NMR parameters determined by averaging over T-sites as outlined in Section 4.3. Orthorhombic hydrated model at saturation (dynamic).

S10 Averaging over T-sites and space group transformations

The average NMR parameters obtained for T1 and T2 labels that can be compared to experiment in the orthorhombic case are derived as follows. The chemical shifts can be averaged out directly for T1 and T2 labels, as they only depend on the trace of the shielding tensors which is invariant to rotations of the tensor. The average T1 and T2 chemical shifts are therefore simply the average of the time-average chemical shifts of each of the

atoms within the T1 respectively the T2 label. However, in deriving average quadrupolar parameters, it is important to consider the different relative orientations of the tetrahedrons within one crystallographic label. The quadrupolar parameters have to be calculated from a single EFG tensor that is representative for the T1 and T2 sites. To obtain such an average, we select reference orientations within the T1 and T2 labels and transform all other tensors to these reference orientations before averaging the tensors to a single tensor per T1/T2 label. These symmetry transformations are derived from the space group $Pmn2_1$ and are detailed in Figure S13. In reality, the orientation of the tensor will slightly differ from the perfect orientation in the unit cell throughout the dynamic run. The EFG tensors V of the aluminium sites should then be transformed with the (inverse) transformation using:

$$V' = R^T V R \quad (8)$$

where V' is the tensor after rotation, for which the orientation coincides with the orientation of the reference site. After doing this for each atom within the T1 and T2 labels, the tensors are averaged per label, and the resulting average T1 and T2 EFG tensors are diagonalised to calculate the C_Q and η_Q parameters.

S11 Structural models and input files

The following files can be provided as additional information via zip:

- **Folder structures:** Crystallographic information files (`.cif`) obtained through PXRD for the dehydrated triclinic system and the as-synthesised orthorhombic system.
- **Folder structures/static:** Initial structures for anhydrous triclinic and saturated orthorhombic systems before structural optimization, in VASP `POSCAR` format. VASP input files for optimization (`INCAR_opt`) and for the linear response NMR calculation

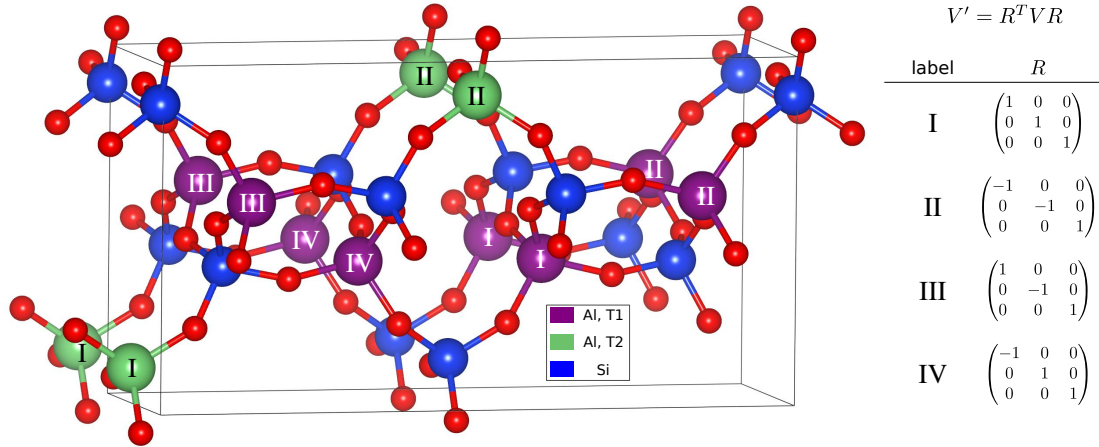


Figure S13: Framework of JBW (extraframework species not shown) with symmetry labels *I* trough *IV* and the corresponding transformation matrix R .

(`INCAR_nmr`). VASP file `KPOINTS` defining the K-point grid for both orthorhombic and triclinic system.

- Folder `structures/dynamic`: Initial structures for anhydrous triclinic and saturated orthorhombic systems in `xyz`-format and CP2K input file `input_md.inp` to perform molecular dynamics in the NPT ensemble.

References

- (1) Harris, R. K.; Becker, E. D.; Cabral de Menezes, S. M.; Goodfellow, R.; Granger, P. NMR Nomenclature: Nuclear Spin Properties and Conventions for Chemical Shifts - IUPAC Recommendations 2001. *Solid State Nucl. Magn. Reson.* **2002**, *458–483*.
- (2) Mortensen, J. J.; Hansen, L. B.; Jacobsen, K. W. Real-space grid implementation of the projector augmented wave method. *Phys. Rev. B* **2005**, *71*, 035109.
- (3) Larsen, A. H. et al. The atomic simulation environment—a Python library for working with atoms. *Journal of Physics: Condensed Matter* **2017**, *29*, 273002.
- (4) Larsen, A. H.; Vanin, M.; Mortensen, J. J.; Thygesen, K. S.; Jacobsen, K. W. Localized atomic basis set in the projector augmented wave method. *Phys. Rev. B* **2009**, *80*, 195112.
- (5) Verstraelen, T.; Vandenbrande, S.; Heidar-Zadeh, F.; Vanduyfhuys, L.; Van Speybroeck, V.; Waroquier, M.; Ayers, P. W. Minimal Basis Iterative Stockholder: Atoms in Molecules for Force-Field Development. *J. Chem. Theory Comput.* **2016**, *12*, 3894–3912.
- (6) Rappe, A. K.; Casewit, C. J.; Colwell, K. S.; Goddard, W. A.; Skiff, W. M. UFF, a full periodic table force field for molecular mechanics and molecular dynamics simulations. *J. Am. Chem. Soc.* **1992**, *114*, 10024–10035.
- (7) Jorgensen, W. L.; Chandrasekhar, J.; Madura, J. D.; Impey, R. W.; Klein, M. L. Comparison of simple potential functions for simulating liquid water. *The Journal of Chemical Physics* **1983**, *79*, 926–935.
- (8) Goeminne, R.; Krause, S.; Kaskel, S.; Verstraelen, T.; Evans, J. D. Charting the Complete Thermodynamic Landscape of Gas Adsorption for a Responsive Metal–Organic Framework. *J. Am. Chem. Soc.* **2021**, *143*, 4143–4147.

- (9) Blöchl, P. E. Projector augmented-wave method. *Phys. Rev. B* **1994**, *50*, 17953–17979.
- (10) Kresse, G.; Joubert, D. From ultrasoft pseudopotentials to the projector augmented-wave method. *Phys. Rev. B* **1999**, *59*, 1758–1775.
- (11) Lippert, G.; Hutter, J.; Parrinello, M. A hybrid Gaussian and plane wave density functional scheme. *Mol. Phys.* **1997**, *92*, 477–487.
- (12) Kühne, T. D. et al. CP2K: An electronic structure and molecular dynamics software package - Quickstep: Efficient and accurate electronic structure calculations. *J. Chem. Phys.* **2020**, *152*, 194103.
- (13) Nosé, S. A unified formulation of the constant temperature molecular dynamics methods. *The Journal of Chemical Physics* **1984**, *81*, 511–519.
- (14) Nosé, S. A molecular dynamics method for simulations in the canonical ensemble. *Molecular Physics* **1984**, *52*, 255–268.
- (15) Perdew, J. P.; Burke, K.; Ernzerhof, M. Generalized Gradient Approximation Made Simple. *Phys. Rev. Lett.* **1996**, *77*, 3865–3868.
- (16) Zhang, Y.; Yang, W. Comment on “Generalized Gradient Approximation Made Simple”. *Phys. Rev. Lett.* **1998**, *80*, 890–890.
- (17) Grimme, S.; Antony, J.; Ehrlich, S.; Krieg, H. A consistent and accurate *ab initio* parametrization of density functional dispersion correction (DFT-D) for the 94 elements H-Pu. *The Journal of Chemical Physics* **2010**, *132*, 154104.
- (18) Grimme, S.; Ehrlich, S.; Goerigk, L. Effect of the damping function in dispersion corrected density functional theory. *J. Comput. Chem.* **2011**, *32*, 1456–1465.
- (19) VandeVondele, J.; Hutter, J. Gaussian basis sets for accurate calculations on molecular systems in gas and condensed phases. *The Journal of Chemical Physics* **2007**, *127*, 114105.

- (20) Pickard, C. J.; Mauri, F. All-electron magnetic response with pseudopotentials: NMR chemical shifts. *Phys. Rev. B* **2001**, *63*, 245101.
- (21) Kresse, G.; Hafner, J. *Ab initio* molecular dynamics for liquid metals. *Phys. Rev. B* **1993**, *47*, 558–561.
- (22) Kresse, G.; Hafner, J. *Ab initio* molecular-dynamics simulation of the liquid-metal–amorphous-semiconductor transition in germanium. *Phys. Rev. B* **1994**, *49*, 14251–14269.
- (23) Kresse, G.; Furthmüller, J. Efficiency of ab-initio total energy calculations for metals and semiconductors using a plane-wave basis set. *Computational Materials Science* **1996**, *6*, 15–50.
- (24) Kresse, G.; Furthmüller, J. Efficient iterative schemes for *ab initio* total-energy calculations using a plane-wave basis set. *Phys. Rev. B* **1996**, *54*, 11169–11186.
- (25) Monkhorst, H. J.; Pack, J. D. Special points for Brillouin-zone integrations. *Phys. Rev. B* **1976**, *13*, 5188–5192.
- (26) Han, O. H.; Timken, H. K. C.; Oldfield, E. Solid-state “magic-angle” sample-spinning nuclear magnetic resonance spectroscopic study of group III–V (13–15) semiconductors. *The Journal of Chemical Physics* **1988**, *89*, 6046–6052.
- (27) Rocha, J. Direct observation of highly distorted hexa-coordinated aluminium in analusite by very fast ^{27}Al MAS NMR. *Chem. Commun.* **1998**, 2489–2490.
- (28) Müller, D.; Gessner, W.; Samoson, A.; Lippmaa, E.; Scheler, G. Solid-state aluminium- 27 nuclear magnetic resonance chemical shift and quadrupole coupling data for condensed AlO_4 tetrahedra. *J. Chem. Soc., Dalton Trans.* **1986**, 1277–1281.
- (29) Park, M. B.; Vicente, A.; Fernandez, C.; Hong, S. B. Solid-state NMR study of various

- mono- and divalent cation forms of the natural zeolite natrolite. *Phys. Chem. Chem. Phys.* **2013**, *15*, 7604.
- (30) Massiot, D. Sensitivity and Lineshape Improvements of MQ-MAS by Rotor-Synchronized Data Acquisition. *Journal of Magnetic Resonance, Series A* **1996**, *122*, 240–244.
- (31) Neuhoff, P. S.; Kroeker, S.; Du, L.-S.; Fridriksson, T.; Stebbins, J. F. Order/disorder in natrolite group zeolites: A ^{29}Si and ^{27}Al MAS NMR study. *American Mineralogist* **2002**, *87*, 1307–1320.
- (32) Stebbins, J. F.; Burnham, C. W.; Bish, D. L. Tetrahedral disorder in fibrolitic sillimanite: Comparison of ^{29}Si NMR and neutron diffraction data. *American Mineralogist* **1993**, *78*, 461–464.
- (33) Xue, X.; Stebbins, J. ^{23}Na NMR chemical shifts and local Na coordination environments in silicate crystals, melts and glasses. *Phys Chem Minerals* **1993**, *20*.
- (34) Profeta, M.; Mauri, F.; Pickard, C. J. Accurate First Principles Prediction of ^{17}O NMR Parameters in SiO_2 : Assignment of the Zeolite Ferrierite Spectrum. *J. Am. Chem. Soc.* **2003**, *125*, 541–548.
- (35) Lewis, D. W.; Willock, D. J.; Catlow, C. R. A.; Thomas, J. M.; Hutchings, G. J. De novo design of structure-directing agents for the synthesis of microporous solids. *Nature* **1996**, *382*, 604–606.
- (36) Asselman, K.; Radhakrishnan, S.; Pellens, N.; Vinod Chandran, C.; Houlleberghs, M.; Xu, Y.; Pulinthanathu Sree, S.; Kirschhock, C. E. A.; Breynaert, E. K,Na-JBW, a zeolite exhibiting exceptional framework ordering and flexibility. Published online. doi: 10.1021/acs.chemmater.2c01059.

(37) Breynaert, E.; Asselman, K.; Radhakrishann, S. Replication data for: "HSIL based synthesis of ultra-crystalline K_xNa-JBW, a zeolite exhibiting exceptional framework ordering and flexibility. Harvard Dataverse, V1, UNF:6:ntRwJFlAnGwdsz3geMDBtQ. doi: 10.7910/DVN/EPXWYA.